Nonreciprocal Electromagnetically Induced Unidirectional Absorption Based on the Quasi-Periodic Metastructure and Its Application for Permittivity Sensing

Li Zeng, Bing-Xiang Li, and Hai-Feng Zhang

***Abstract*— Nonreciprocal unidirectional absorption, as a critical feature in both applications of military and civilian, has always been a challenging research topic. Here, we introduce a linear incremental arrangement into the formation of the electromagnetically induced absorption (EIA) in a single metastructure unit, creating an asymmetry spatial modulation for the nonreciprocal electromagnetic responses. A unidirectional EIA peak with a high absorption reaching 87.87% is observed for the forward case, and nearly all the incident energy is reflected in the backward case. The maximum isolation ratio (IR) between the forward and backward absorptions is 10.79 dB. To obtain a higher forward absorption and enlarge the IR, an improved nonreciprocal metastructure array is proposed and experimentally demonstrated by applying a linear quasi-periodic array configuration. The forward electromagnetically induced unidirectional absorption is enhanced to 99.53% with an IR of 12.73 dB. The near-perfect absorption provides a promising platform for permittivity sensing, and the measurement of common microwave plates with different relative permittivity shows an excellent linear regression. Such an implementation innovatively combines the asymmetric spatial modulation with EIA to form unidirectional absorption, offering a new guideline for novel nonreciprocal devices, and possessing considerable practical applications in the wireless communication system, ultrasensitive sensing, one-way invisibility, and absorptive switching.**

***Index Terms*— Electromagnetically induced absorption (EIA), nonreciprocal unidirectional absorption, permittivity sensing, quasi-periodic metastructure.**

I. Introduction

NONRECIPROCITY refers to the different electromagnetic loss, phase shift, and other characteristics that occurred in the transmission of electromagnetic waves along with two opposite propagation directions [1], [2], [3], which have wide and significant applications in modern communication, radar, and electronic countermeasure technology. Frequently used microwave nonreciprocal components include isolators, circulators, gyrators, phase shifters, and switches [4], [5], [6], but their dominant implementations rely on the high-resistivity ferrimagnetic materials, such as the yttrium–iron–garnet or the compounds of iron oxides [7], [8]. However, such methods using magnetic materials or applying an external magnetic field bias to break the inverse symmetry in time or space often suffer from major drawbacks, such as being bulky, high-loss, expensive, inconvenient to integrate, and sensitive to temperature. With the increasing demand for miniaturization and low power consumption in the development of communication devices, the research of simultaneous transceiver nonreciprocal devices on the nonmagnetization, integration, and high isolation has been a hot priority topic for scholars in related fields at home and abroad. In 2011, Kodera et al. [9] proposed a metamaterial structure loaded by semiconductor-based isolators to produce Faraday rotation. Due to the presence of the isolators, nonreciprocal transmission responses were obtained for the different ports without static magnetic field bias. In 2014, Shen et al. [10] proposed a scheme to realize the unidirectional invisibility phenomenon using a double-layer nonparity-time symmetric flat plate structure. Their numerical calculations claimed that the unidirectional invisibility phenomenon can be observed in the conventional double-layer plate structure with different real parts of the refractive index when the imaginary part of the refractive index and the thickness of the plate meets appropriate conditions. In 2017, Bai et al. [11] realized the unidirectional nonreciprocal absorption at the exceptional point by accumulating different phase shifts in both vertical and horizontal directions of two gold nanorods. In addition, nonreciprocal propagation can be achieved not only for electromagnetic waves but also for acoustic waves. Li et al. [12] experimentally built the sound unidirectional transmission in a sonic-crystal-based acoustic diode, and He et al. [13] adopted the asymmetric grating to achieve a similar nonreciprocal phenomenon, providing valuable applications for acoustic rectifiers and acoustic diodes.

Electromagnetically induced absorption (EIA), as a kind of constructive interference between the transition channels in the four-level atomic system, has attracted many investigations due

Manuscript received 2 September 2022; revised 23 December 2022; accepted 9 January 2023. Date of publication 1 February 2023; date of current version 3 February 2023. This work was supported in part by the National Key Research and Development Program of China under Grant 2022YFA1405000 and in part by the Postgraduate Research & Practice Innovation Program of Jiangsu Province under Grant KYCX21_0720. The Associate Editor coordinating the review process was Seyed Hossein Hesamedin Sadeghi. *(Corresponding authors: Bing-Xiang Li; Hai-Feng Zhang.)*

The authors are with the College of Electronic and Optical Engineering and the College of Flexible Electronics (Future Technology), Nanjing University of Posts and Telecommunications, Nanjing 210023, China (e-mail: 2238089728@qq.com; bxli@njupt.edu.cn; hanlor@163.com).

Digital Object Identifier 10.1109/TIM.2023.3239641

1557-9662 © 2023 IEEE. Personal use is permitted, but republication/redistribution requires IEEE permission.
See https://www.ieee.org/publications/rights/index.html for more information.

Authorized licensed use limited to: Nanjing Univ of Post & Telecommunications. Downloaded on February 08,2023 at 07:48:04 UTC from IEEE Xplore. Restrictions apply.

to its intriguing phenomena, such as anomalous dispersion and accelerating the group delay time [14], [15], [16]. However, in the conventional quantum interference and coherent systems, the occurrence conditions of EIA are extremely harsh, often requiring an ultralow temperature close to absolute zero and a high-intensity laser, whose costly implementation and uncontrollable experimental environment greatly limit the applications of EIA in practical engineering. Recently, with the proposal of metastructures, such as the metamaterial and metasurface, people have found a new way to manipulate electromagnetic waves in the desired manner due to the unusual and exotic electromagnetic properties of metastructures [17], [18], [19]. The emergence of metastructures breaks through the above limitations and provides a promising platform for the analogy studies of the quantum-classical system. Owing to the controllable parameters and relaxed experimental environment, the theoretical prediction of EIA, which is difficult to be observed in a quantum system, could be verified relatively easily in the metastructure system. There is no doubt that the ideas of quantum physics have brought deep insights and potential applications to the metastructures, and the development of metastructures can also contribute back to inspire the research of quantum systems [20], [21]. The currently reported implementations of the EIA effect mainly include introducing an intermediate retardation-induced phase shift in the two-coupled-resonator system [22], [23], using the three-resonator coupling system [24], and stimulating by oblique incidence [25]. Nevertheless, there are still several challenges hindering the development of metastructure-based EIA. First, almost all studies of the EIA exhibit the reciprocal electromagnetic response, which also implies a large number of significant nonreciprocal application fields are unexplored, such as one-way stealth, electromagnetic shielding, switchable fast/slow wave devices, and absorption-based isolator and photodiodes. Second, the reported absorption efficiency of the EIA effect is too poor to be applied in complex electromagnetic environments, and an effective method for enhancing the absorption is still urgently desired at this stage. Third, most realizations of the EIA metastructures need to introduce phase delays in vertical space for the interference of the coupled system, which leads to the drawbacks of bulky dimensions and difficult integration. In addition, the majority of research on EIA is focused on the terahertz and optical bands [26], [27], [28], but explorations in the microwave band are still relatively rare.

As a primary way of acquiring information during the detecting, identifying, and testing processes of materials, permittivity sensors have long been a hot research topic, and diverse implementations have emerged for enriching various applications in such an information era, such as waveguide cavities [29], [30], coaxial probes [31], [32], planar resonators [33], [34], [35], and sandwiched resonator structures [36], [37]. In 2007, De Vos et al. [38] demonstrated a highly miniaturized optical label-free biosensor based on a Silicon-on-Insulator microring cavity. Thanks to its extremely small dimension, this device performs outstandingly in terms of absolute molecular mass sensing. However, the performance for bulk refractive index changes is moderate theoretically. Despite being commercially available for laboratory use, the technique suffers from high measurement error. In 2019, a high-sensitive microwave microfluidic sensor based on the planar split ring resonator is proposed by Govind and Akhtar [39] for detecting glucose concentration in aqueous glucose solutions. The sensitivity for glucose testing is found to be 0.026 MHz/mgdl^{-1}, a fair improvement compared to conventional sensors with similar sensing methodologies. In 2021, Aydinalp's group [40] investigates the sensing depth of a 2.2-mm-diameter open-ended coaxial probe for skin cancer detection. The effect of tissue heterogeneity on measurement accuracy can be decreased by quantifying the probe sensing depth. Among the plausible advantages of microwave planar sensors is that they have a compact size, a low cost, and ease of fabrication and integration compared to prevailing sensors.

The development of modern sensing equipment is gradually tending to be integrated, digital, intelligent, and multifunctional for adapting to the surging complex electromagnetic environment. The coping ability of conventional permittivity sensors with a single function is gradually being stretched to the limit, and increasing the type and number of sensing or other electromagnetic devices may suffer the problem of electromagnetic compatibility between different systems. Therefore, designing a new generation of composite sensors with multitask ability has attracted burgeoning attention in wireless communication, cosmic exploration detection, and medical diagnosis system. When reviewing the existing reports, we could learn that the research on the multifunctionalization of sensors still remains huge empty pages waiting for new design inspirations to fill. Nonreciprocity, as an extraordinary electromagnetic property both in the microwave and optical frequency, has raised in myriad significant applications in satellite communication [41], digital encoding [42], and multifunctional integration [43], which provides a composite platform that allows for compatible with sensing capability and other features. This opens up new possibilities and design concepts for developing multitasking, digital, and intelligent devices.

In this article, by introducing a linear incremental arrangement that acted like an asymmetric waveguide into the design of bright-dark-mode theory, a nonreciprocal phenomenon of the forward electromagnetically induced unidirectional absorption (EIUA) and backward electromagnetically induced reflection (EIR) has been successfully observed in a microwave metastructure unit. To further obtain a higher forward absorption efficiency, five proposed metastructure units are adopted to constitute a 1-D array in a linear quasi-periodic arrangement. The forward absorption is enhanced from 87.87% to 99.53%, and the system isolation ratio (IR) reaches 12.73 dB. Meanwhile, such a near-perfect EIUA provides a feasible and excellent platform for permittivity sensing, which is experimentally demonstrated by measuring four common microwave plates with different relative permittivities in this article. A good agreement between the simulated and measured results is obtained. Therefore, three functions are integrated

Authorized licensed use limited to: Nanjing Univ of Post & Telecommunications. Downloaded on February 08,2023 at 07:48:04 UTC from IEEE Xplore. Restrictions apply.

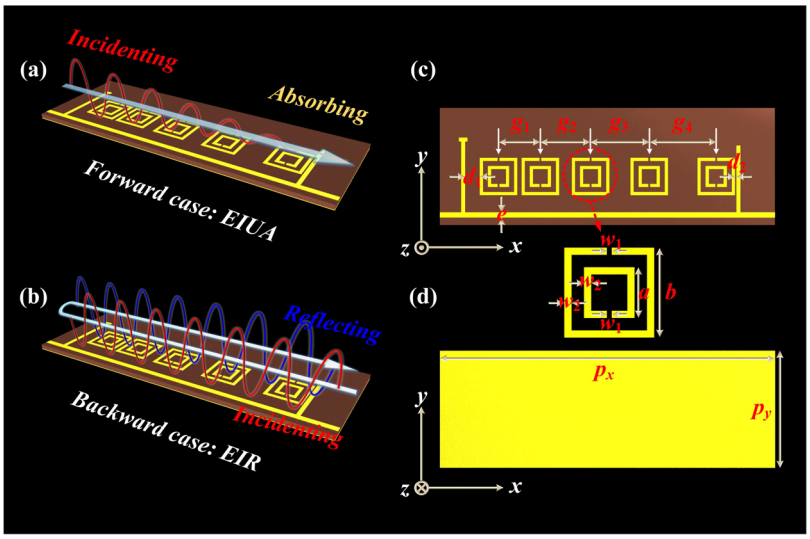

Fig. 1. Schematic configuration of the nonreciprocal metastructure unit with the concept schematic of (a) forward EIUA and (b) backward EIR. (c) Top view and (d) Back view of the proposed nonreciprocal metastructure unit with the enlarged illustration of the NSR. The marked parameters: $a = 5$ mm, $b = 8.9$ mm, $d_1 = 3.55$ mm, $d_2 = 0.4$ mm, $e = 1.2$ mm, $g_1 = 9.2$ mm, $g_2 = 11.04$ mm, $g_3 = 12.88$ mm, $g_4 = 14.72$ mm, $p_x = 80$ mm, $p_y = 28$ mm, $w_1 = 0.5$ mm, and $w_2 = 0.7$ mm.

into one single device to deal with various electromagnetic tasks from positive or negative information sources, in which two are energy absorption and permittivity sensing under the forward incidence, and one is reflective filtering under the backward incidence.

II. Structural Design and Results of Nonreciprocal Metastructure Unit

Here, first, we present the schematic configuration of the nonreciprocal metastructure unit in Fig. 1, which realizes the forward EIUA and the backward EIR, respectively, as shown in Fig. 1(a) and (b). The unit is established on an FR4-epoxy substrate (relative permittivity: 4.4 and loss tangent: 0.02) [44] backed by a full copper ground, and the top layer is mainly composed of a T-shaped copper resonator, an I-shaped copper resonator, and a series of specially arranged copper nested split rings (NSRs) between them. The thicknesses of the FR4-epoxy substrate and copper layers are identified as 1.2 and 0.035 mm, respectively. The left T-shaped resonator and the right I-shaped resonator are directly connected to the transverse transmission channel near the bottom, which allows direct excitation by the transverse transmission channel. As the locations of the NSRs are relatively distant from the transmission channel and the splitting directions are perpendicular to the transmission channel, the NSRs can only be indirectly excited by the T-shaped resonator and the I-shaped resonator through near-field coupling. Therefore, the T-shaped resonator, the I-shaped resonator, and NSRs are defined as the bright resonator 1, bright resonator 2, and dark resonators, respectively.

The individual responses of the S-parameters for the T-shaped resonator, the I-shaped resonator, and a single NSR are given in Fig. 2 under the forward case. From Fig. 2(a) and (b), we can see that the directly connected T-shaped resonator can excite an electric resonance at 2.24 GHz with a broad full-width at half-maximum (FWHM), and the I-shaped resonator induces a similar electric resonance

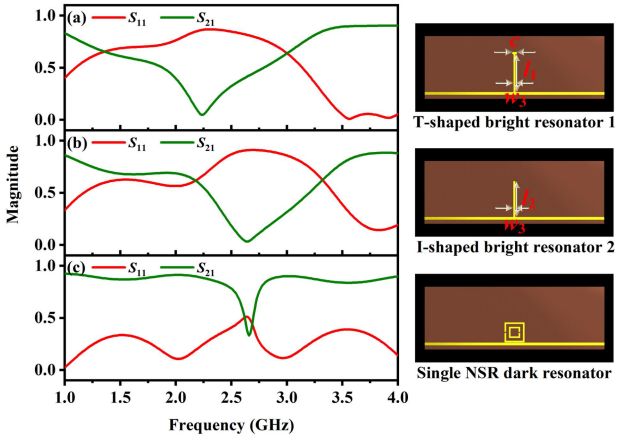

Fig. 2. Individual responses of the S-parameters (S_{11} and S_{21}) for (a) T-shaped resonator, (b) I-shaped resonator, and (c) single NSR paralleled to the transmission channel under the forward case. The marked parameters: $c = 2$ mm, $l_1 = 17$ mm, $l_2 = 16$ mm, and $w_3 = 0.9$ mm.

in the vicinity of 2.65 GHz. As for the NSR, the situation when the splitting direction is paralleled to the transmission channel is simulated for analogizing the coupling from the bright mode in the near-field, and it can be seen that a magnetic resonance with narrow FWHM is generated at 2.66 GHz.

To obtain the nonreciprocal response, a linear incremental distance is purposely introduced into each neighboring NSR to break the spatial structural symmetry. Fig. 1(c) schematically displays the described arrangement. The separations of five NRS along the x-axis are increased as a linear function $g(i) = g_1 + k_1 \times g_1 \times (i\text{-}1)$ ($i = 1, 2, 3$, and 4), where $g_1 = 9.2$ mm is the first separation between the center of the first NSR and second NSR, and $k_1 = 0.2$ is the linear growth coefficient for the subsequent separations of $g_2 = 11.04$ mm, $g_3 = 12.88$ mm, and $g_4 = 14.72$ mm. The design idea of using exponential function has similar validity that has been verified by the experiment of asymmetric light propagation in the photonic crystal waveguides [45] to generate similar

Authorized licensed use limited to: Nanjing Univ of Post & Telecommunications. Downloaded on February 08,2023 at 07:48:04 UTC from IEEE Xplore. Restrictions apply.

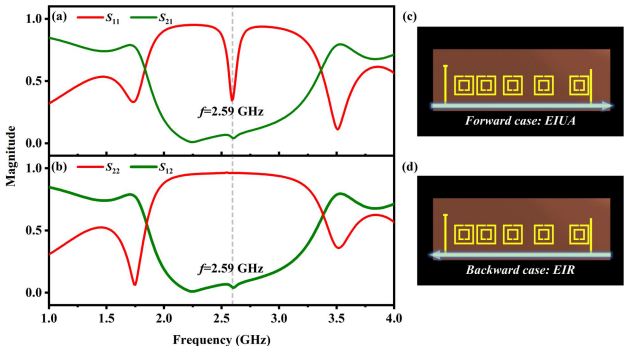

Fig. 3. (a) S-parameters (S_{11} and S_{21}) of the combined metastructure unit for the forward cases and (b) S-parameters (S_{22} and S_{12}) for the backward case, where the illustrations are the schematics of (c) forward and (d) backward functions.

nonreciprocal phenomenon but suffering from several realistic dilemmas, which is also one of the past design schemes. If a smaller number of NSRs are selected, the separations between NSRs would be small and close in values, which makes it difficult to construct enough spatial asymmetry to generate the nonreciprocity phenomenon. On the other hand, if the number of NSRs exceeds a certain threshold, the separations between NSRs would be enlarged dramatically, leading to severely surging device size and fabricated cost. It would be a tough and constrained decision to balance the nonreciprocal performance and device size under the exponential function. The linear increasing function provides a smoother growth trend and more flexible compatibility for both performance optimization and fabrication requirements. Considering the above-mentioned advantages and disadvantages, we applied the linear increasing function in this work for inducing the nonreciprocal unidirectional absorption.

When the T-shaped resonator, the I-shaped resonator, and five NSRs are integrated on the same substrate, the bright electric resonances, and dark magnetic resonance interference constructively with each other, a remarkable EIA effect will be generated by purposely adjusting the interference position between them. Fig. 3(a) provides the S-parameters (S_{11} and S_{21}) for the forward incidence, and we can observe that S_{21} forms a broad stopband, inside which an S_{11} dip passes through its minimum of 0.345 at 2.59 GHz. Such a phenomenon is quite different in the backward case, whose S-parameters (S_{22} and S_{12}) are plotted in Fig. 3(b). The S_{11} dip obtained in the forward case completely vanished, remaining only the functionality of broadband electromagnetically induced reflective filter from 2.02 to 3.14 GHz with S_{22} above 0.9.

The physical mechanism for such a nonreciprocal phenomenon can be interpreted by the electric field distributions and phase distributions at 2.59 GHz under the forward and backward incidence in Fig. 4. When the electric field propagates along $+x$-direction, the T- and I-shaped bright resonators in Fig. 4(a) are strongly excited in the reverse phase, which is equivalent to the aggregations of the positive and negative charges and similar to the trapped mode distribution [46], [47], [48], as marked in Fig. 4(b). The field leaked from the bright resonators induces the inspiration of five dark resonators, and we can notice that the field amplitude on each NSR follows a gradual weakening phenomenon along the forward transmission path. Such observations signify that the asymmetrical arrangement of five NSRs acts as an asymmetric waveguide, and the field energy can be coupled from the bright resonator 1 to the bright resonator 2 through this asymmetric waveguide in the forward case. Three types of resonators are strongly interfering with each other, and as a result, the antiphase aggregations of the electric field strongly trap and cancel out the incident energy before the receiving port on the right; thus, a high absorption peak is rising. In the backward propagation case along the $-x$-direction, only the right I-shaped bright resonator is excited, and we can see that the field energy is blocked from entering this asymmetrical waveguide on the right-hand side. The interference with the dark resonators and the left T-shaped bright resonator is cut off, so the incident energy is reflected in the source port, which is also consistent with the electrical resonance properties of a single dipole excitation.

Fig. 5(a) calculates the forward absorption A_{forward} and the backward absorption A_{backward} by (2) and (3), and it is apparent that an 87.87% absorption peak is generated at 2.59 GHz for the forward case, where the absorption for the backward case at the same frequency is 7.33%. Moreover, the forward and backward phase responses are given in Fig. 5(b), and two abrupt slope reversals can be observed around 2.59 GHz under the forward case, indicating an effect termed anomalous dispersion in classical physics, which is one of the signature features of the EIA and has been widely exploited in the applications of accurate sensing and superluminal group velocities [49], [50]. These phenomena of amplitude attenuation and phase reversal well confirm the generation of EIA under the forward case. To quantitatively describe the nonreciprocity, the IR and contrast ratio (CR) calculated by (3) and (4) [3] are introduced in Fig. 5(c), which implies the absorption difference between the forward port and the backward port. The maximum IR reaches 10.79 dB at the target frequency of 2.59 GHz, corresponding to a CR of 0.846

$$\begin{aligned} A_{\text{Forward}}(\omega) &= 1 - R_{\text{Forward}}(\omega) - T_{\text{Forward}}(\omega) \\ &= 1 - S_{11}^2 - S_{21}^2 \end{aligned} \tag{1}$$

$$\begin{aligned} A_{\text{Backward}}(\omega) &= 1 - R_{\text{Backward}}(\omega) - T_{\text{Backward}}(\omega) \\ &= 1 - S_{22}^2 - S_{12}^2 \end{aligned} \tag{2}$$

$$\text{IR} = 10\log_{10}\left(\frac{A_{\text{Forward}}}{A_{\text{Backward}}}\right) \tag{3}$$

$$\text{CR} = \left(\frac{A_{\text{Forward}} - A_{\text{Backward}}}{A_{\text{Forward}} + A_{\text{Backward}}}\right). \tag{4}$$

The coupled oscillator model is introduced to investigate the generation mechanism of the EIA phenomenon at 2.59 GHz. The theoretical system exhibited in Fig. 6(a) is described by the classical coupled Lorentz second-order differential equations of (5) and (6) [23]

$$\text{x''}_1(t) = \gamma_1 \text{x'}_1(t) + \omega_1^2 \text{x}_1(t) - \kappa' \text{x}_2(t) = f'(t) \tag{5}$$

$$\text{x''}_2(t) = \gamma_2 \text{x'}_2(t) + \omega_2^2 \text{x}_2(t) - \kappa' \text{x}_1(t) = 0 \tag{6}$$

where oscillator 1 and oscillator 2 represent the radiation path 1 from the bright resonator 1 to the dark resonators

Authorized licensed use limited to: Nanjing Univ of Post & Telecommunications. Downloaded on February 08,2023 at 07:48:04 UTC from IEEE Xplore. Restrictions apply.

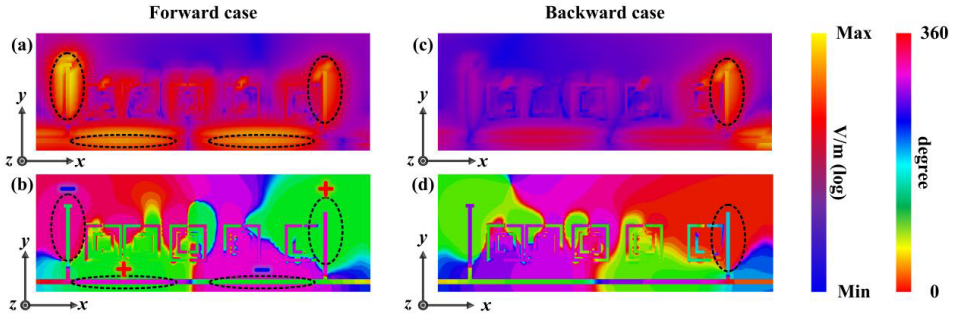

Fig. 4. Electric field distributions at 2.59 GHz for (a) forward incidence and (c) backward incidence and the phase distributions at 2.59 GHz for (c) forward incidence and (d) backward incidence.

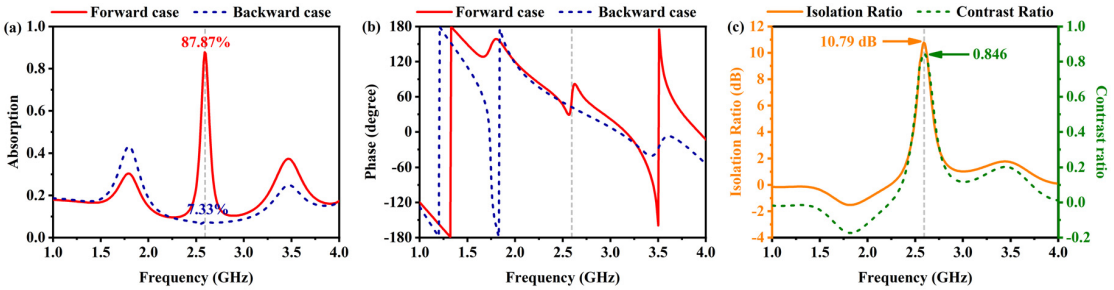

Fig. 5. (a) Forward absorption and backward absorption. (b) Forward phase and backward phase. (c) Calculated IR and CR.

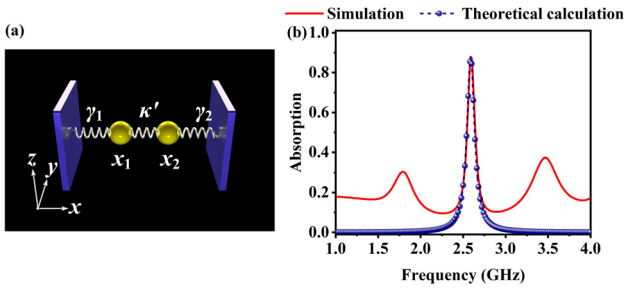

Fig. 6. (a) Mechanical schematic of the theoretical coupled oscillator model with a coupling connection of $\kappa' = \kappa e^{i\omega t}$, and (b) comparisons of the EIA effect between the simulation and theoretical calculation. In the theoretical calculation, $\omega_0 = 2.59$ GHz, $\delta = 1$ GHz, $\gamma_1 = 0.108$ GHz, $\gamma_1 = 0.02$ GHz, and $\kappa = 0.1$ GHz.

and the radiation path 2 from the dark resonators to the bright resonator 2, respectively. x_1 and x_2 are defined as the respective displacements of two oscillators with respect to their equilibrium positions. γ_1 and γ_2 are the damping constants for oscillator 1 and oscillator 2, and the interactive coupling coefficient is adopted in the complex form of $\kappa' = \kappa e^{i\varphi}$, which is crucial to the phase retardation effect between two contributing oscillators.

Only the left oscillator can be directly excited by the power source of the forward transmitting energy $f'(t)$, and the right oscillator needs an indirect coupling connection κ' to drive the generation of EIA. Using the harmonic assumptions of $x_j(t) = a_j e^{-i\omega t}$ and $f'(t) = f' e^{-i\omega t}$, we get the approximation in (8), and furthermore, the supplementary equation for the EIA system can be listed in (8)

$$\omega_j^2 - \omega^2 - i\omega\gamma_j \approx -2\omega_0\left(\omega - \omega_j + \frac{i\omega\gamma_j}{2}\right) = -2\omega_0\Omega_j \quad , \quad j = 1,\ 2 \tag{7}$$

$$\begin{bmatrix} -2\omega_0\Omega_1 & -\kappa' \\ -\kappa' & -2\omega_0\Omega_2 \end{bmatrix}\begin{bmatrix} a_1 \\ a_2 \end{bmatrix} = \begin{bmatrix} f' \\ 0 \end{bmatrix}. \tag{8}$$

After the matrix inversion, the solution is deduced as follows:

$$\begin{bmatrix} a_1 \\ a_2 \end{bmatrix} = \frac{1}{\kappa'^2 - 4\omega_0^2\Omega_1\Omega_2}\begin{bmatrix} 2\omega_0\Omega_2 f' \\ -\kappa' f' \end{bmatrix}. \tag{9}$$

The final absorption of this EIA system is calculated from the imaginary of the solution of the coupled differential equations, representing the dissipated power, as shown in the following equation [51], [52]:

$$A(\omega) = \mathrm{Im}\left(\frac{2\omega_0\Omega_2 f'}{\kappa'^2 - 4\omega_0^2\Omega_1\Omega_2}\right) \tag{10}$$

where $\Omega_1 = \omega\text{-}\omega_0 + i\gamma_1/2$ and $\Omega_2 = \omega\text{-}\omega_0 + \delta + i\gamma_2/2$.

The comparison of the theoretically calculated absorption from the coupled oscillator model with the simulated results is presented in Fig. 6(b), and we can observe that a sharp absorption peak is generated at 2.59 GHz under the interferential coupling of two oscillators, which keeps high consistency with the simulated result. It is worth pointing out that the proposed coupled oscillator model is an ideal theoretical discussion with no external losses, meaning that it is only applicable to account for the EIA peak at 2.59 GHz arising from the constructive interference between two radiation paths, which is why some mild mismatches are observed for absorption comparison outside 2.45–2.71 GHz, as shown in Fig. 6(b). The electric field distributions of the forward absorption peaks at 1.79 and 3.74 GHz are given in Fig. 7; we can be informed that the weak absorption peak at 1.79 GHz originates from the weak in-phase coupling between the bright resonator 1 and the bright resonator 2, as shown in Fig. 7(a), and the other peak at 3.74 GHz is mainly affected by a weak individual dipole response of the bright resonator 1, as shown in Fig. 7(b). Since no constructive interference occurred at 1.79 and 3.74 GHz,

Authorized licensed use limited to: Nanjing Univ of Post & Telecommunications. Downloaded on February 08,2023 at 07:48:04 UTC from IEEE Xplore. Restrictions apply.

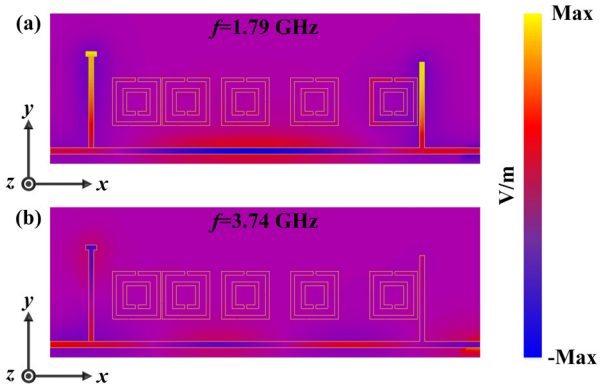

Fig. 7. Electric field distributions at (a) 1.79 and (b) 3.74 GHz under the forward incidence.

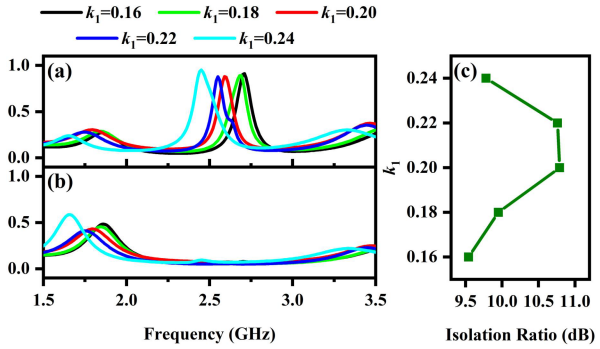

Fig. 8. (a) Forward and (b) backward absorptions varied with different k_1's from 0.16 to 0.24 and (c) their corresponding isolation.

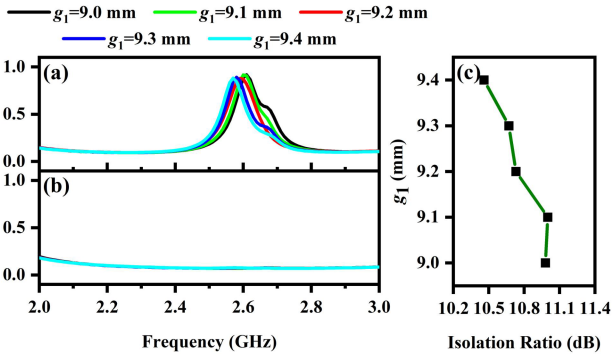

Fig. 9. (a) Forward and (b) backward absorptions varied with different g_1's from 9.0 to 9.4 mm and (c) their corresponding isolation.

it is not hard to find that the overall strength of the electric field at 1.79 and 3.74 GHz are substantially weakened compared with the electric field distribution at 2.59 GHz in Fig. 4. In addition, the high loss tangent in the dielectric substrate also contributes to a certain extent to the out-of-target absorption.

The effects of the linear growth coefficient k_1 and the first based separation g_1 on the forward and backward absorptions are discussed in Figs. 8 and 9. When k_1 increases from 0.16 to 0.24, the enlarging rate of four separations among five NSRs becomes more sharper, and the total length is further extended. We can see that the forward absorption peak is gradually shifted toward the low-frequency region with a weak fluctuation in peak values. The backward absorption curve is slightly bulged when k_1 grows or shrinks out of an

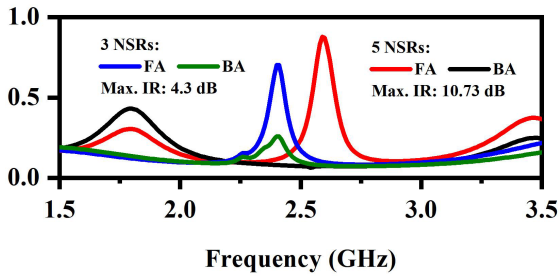

Fig. 10. Forward and backward absorptions when the number of NSRs is 3 and 5, respectively.

appropriate range, which results in a trend of first increasing and then decreasing absorption isolation, reaching a maximum of 10.79 dB at $k_1 = 0.2$. On the other hand, with the diminishing of $g1$, which means the approaching of the first NSR and second NSR, the forward absorption and isolation will get a slight improvement. When $g_1 = 9.0$ mm, only a gap of 0.1 mm is retained between the first NSR and the second NSR. Such a narrow spacing requires a more stringent fabrication process and accuracy, and limits its adaptability, which will not be involved in our practical consideration. Therefore, for a comprehensive consideration of the forward absorption, IR, and fabrication, g_1 and k_1 are determined as 9.2 mm and 0.2 in this article.

Furthermore, the nonreciprocal performance concerning the number of the NSRs is also discussed in Fig. 10, and we can see that, when the number of NSRs is decreased to 3, which means that only two separations exit, it is far from enough for such an arrangement to construct the required spatial asymmetry, and the limited interference path could not provide a matching phase condition required for the coupled oscillator model to induce effective interference and sufficient absorption. These factors contribute to a first enhancing and then weakening behavior of the forward absorption and a contrary behavior of the backward absorption when the number of NSRs is only 3, resulting in lower absorption isolation of 4.3 dB. However, if the number of NSRs exceeds a certain limit, this design would inevitably face the problem of oversizing. After comprehensive consideration of the nonreciprocity performance and device size, five NSRs are adopted in this article.

III. Structural Design and Results of Improved Nonreciprocal Metastructure Array

To further enhance the forward absorption and obtain a larger IR, an improved nonreciprocal metastructure array is experimentally demonstrated by applying a linear quasi-periodic array configuration based on the five metastructure units designed above. The conceptual and fabricated schematic configuration of this nonreciprocal metastructure array is exhibited in Fig. 11. The dielectric substrate is the FR4-epoxy with a thickness of 1.2 mm. The coated metals on the top and bottom layers are copper with a thickness of 0.035 mm. The linear quasi-periodic array configuration is similar to the linear incremental arrangement of the NSRs in a single unit. The separations of five metastructure units are

Authorized licensed use limited to: Nanjing Univ of Post & Telecommunications. Downloaded on February 08,2023 at 07:48:04 UTC from IEEE Xplore. Restrictions apply.

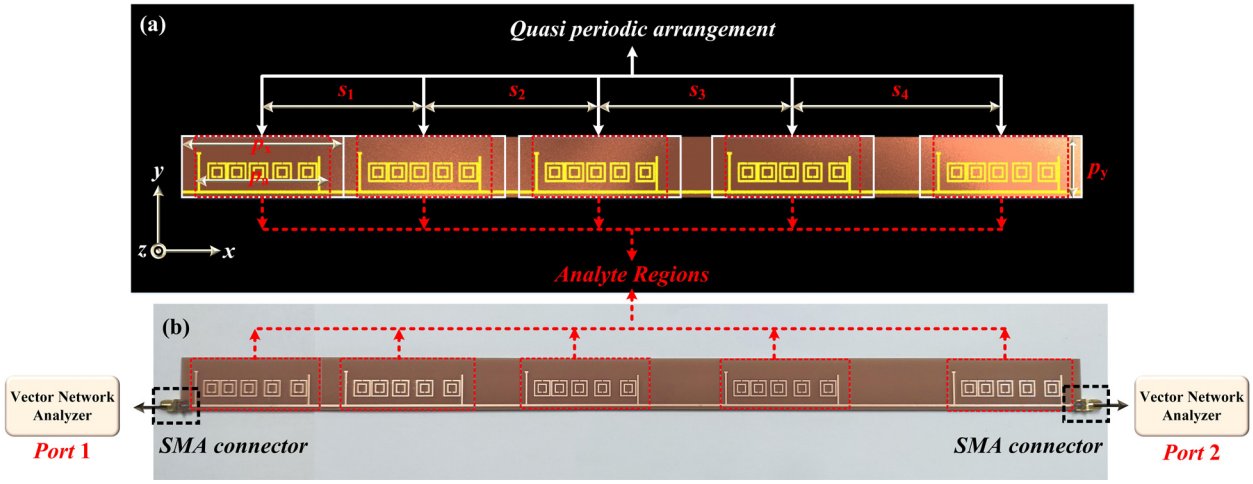

Fig. 11. (a) Schematic configuration of the nonreciprocal metastructure array with the photograph of (b) fabricated sample. The metastructure array is composed of five metastructure units (marked by white rectangular frames) with a linear quasi-periodic array arrangement. The sensing performance of the metastructure array is discussed by measuring the analytes with different permittivity, and the located regions of the analytes are marked by red rectangular frames. The marked structural parameters: $s_1 = 80$ mm, $s_2 = 94.4$ mm, $s_3 = 108.8$ mm, $s_4 = 123.2$ mm, and $p_a = 70$ mm.

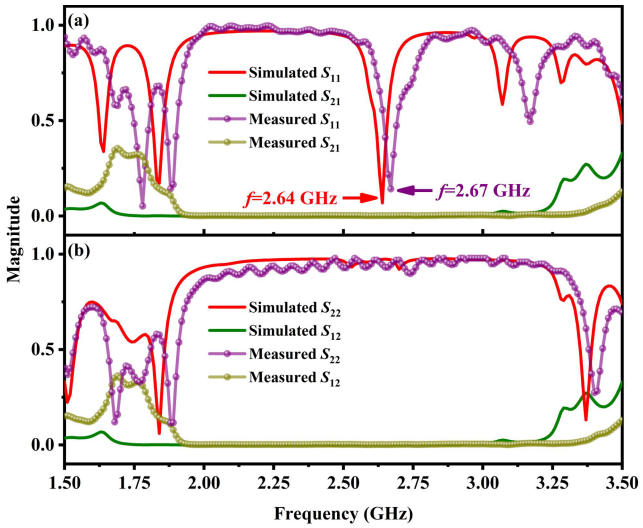

Fig. 12. (a) Simulated and measured S-parameters (S_{11} and S_{21}) of the metastructure array for the forward cases and (b) simulated and measured S-parameters (S_{22} and S_{12}) for the backward case.

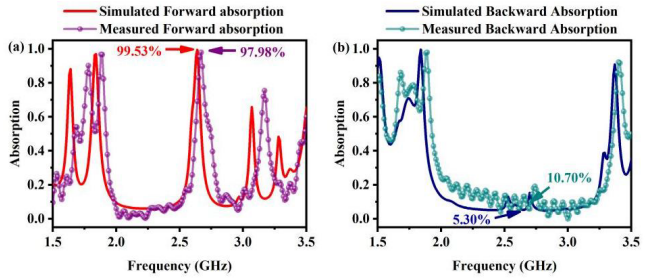

Fig. 13. (a) Simulated and measured forward absorptions of the metastructure array, and (b) simulated and measured backward absorptions.

arranged with a linear function of $s(i) = s_1 + k_2 \times s_1 \times (i\text{-}1)$ ($i = 1, 2, 3$, and 4), where $s_1 = 80$ mm is the first separation between the center of the first unit and the second unit, and $k_2 = 0.18$ is the linear growth coefficient for the subsequent unit separations of $s_2 = 94.4$ mm, $s_3 = 108.8$ mm, and $s_4 = 123.2$ mm. The locations of five metastructure units are marked by the white rectangular frames, as illustrated in Fig. 11(a). Such a configuration builds a nested waveguide array based on an asymmetric waveguide unit to obtain a more enhanced nonreciprocal response between the forward and backward absorptions. The incident forward power and the backward power are radiated and received through the SMA connectors, and the S-parameters of the fabricated array are tested by the vector network analyzer (Keysight e5071c), as shown in Fig. 11(b).

The comparison of the simulated and measured S-parameters of the proposed metastructure array is presented in Fig. 12, where Fig. 12(a) corresponds to the forward case and Fig. 12(b) denotes the backward case. Both Fig. 12(a) and (b) visualize a message that whether S_{12} or S_{21} is completely suppressed to nearly zero in broadband from 1.9 to 3.4 GHz. Such a filtering phenomenon provides a better rectangularity for the reflective stopband, which enables a potential capability for enhancing the anti-interference and detection accuracy of the equipment. For the forward case, the simulated S_{11} resonates at 2.64 GHz with a minimum value of 0.068, resulting in efficient absorption of 99.53%, as calculated in Fig. 13(a). There is a slight frequency shift of 0.03 GHz between the measured S_{11} dip at 2.67 GHz and the simulated one, and the corresponding measured absorption is 97.98%, as shown in Fig. 13(a). Slight measurement tolerance is mainly caused by the structure bending of the relatively long array substrate during the testing process, where the issues brought by the fabrication accuracy and metal oxidation also need to be taken into account as the common contributors to the slight frequency shift. However, from the overall viewpoint, the measured results keep in good agreement with the simulation results, effectively demonstrating the high EIUA characteristics of the proposed metastructure array in the forward case.

For the reverse propagation in Fig. 12(b), the reflection dip has vanished, and a noticeable EIR stopband with excellent rectangularity can be measured in 2.07–3.30 GHz (the relative

Authorized licensed use limited to: Nanjing Univ of Post & Telecommunications. Downloaded on February 08,2023 at 07:48:04 UTC from IEEE Xplore. Restrictions apply.

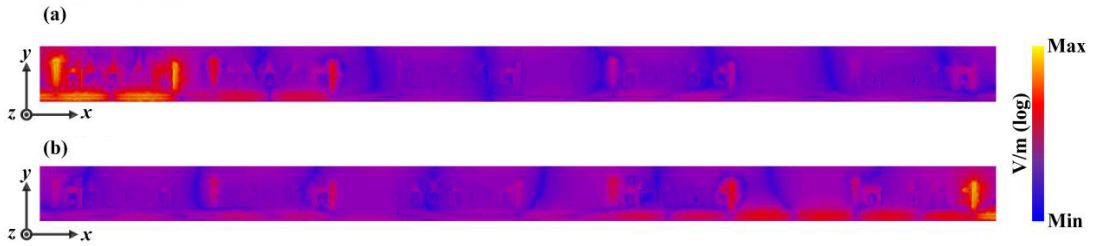

Fig. 14. Electric field distributions at 2.64 GHz for (a) forward case and (b) backward case.

bandwidth is 45.81% for S_{22} >0.9). Similar to the forward case, a slight frequency offset is observed for the measured upper and lower cutoff frequencies of the reflective stopband, but the overall coincidence remains good. The simulated and measured backward absorptions for the target frequency at 2.64 and 2.67 GHz are, respectively, calculated as 5.3% and 10.7%, as shown in Fig. 13(b), where the unstable signal reception (wavy curve) of the vector network analyzer caused by the welding error of the SMA connectors is mostly responsible for the relatively high measured backward absorption. In conclusion, although there are some slight differences between the simulated and measured results, their consistency remains within the expected range, further verifying the feasibility and correctness of this quasi-periodic arrangement technique in the design of nonreciprocal phenomena.

Fig. 14(a) and (b) provides the electric field distributions of the metastructure array for the forward and backward cases at 2.64 GHz. For the forward propagation in Fig. 14(a), the majority of the electric field is concentrated in the first two units, in which the electric field distribution in a single unit is similar to the physical mechanism of EIUA described in Fig. 4(a), and this phenomenon lays the foundation for forward high absorption. Then, observing from an array perspective, with the continued traveling of the electromagnetic waves, the electric field strength begins to decay rapidly and weakly distributes around the output port, indicating the superposition and enhancement of the energy dissipation of electromagnetic waves. This is also proved in Fig. 13(a), where the forward absorption rises by 11.66% from 87.87% to 99.53%. For the backward propagation in Fig. 14(b), the electric field distribution similar to Fig. 4(c) is found in the first unit located near the input port, and when the backward electromagnetic wave passes through this asymmetric quasi-periodic array, the interference between the rightmost unit and the others is further cut off, and the property of single dipole excitation will also be superimposed and strengthened. As a result, a more complete EIR stopband is generated with a better rectangularity.

The simulated and measured IR and CR are calculated in Fig. 15(a) and (b). The introduction of the quasi-periodic array configuration dramatically reinforces the asymmetry of the whole structure, which contributes to the intensification of the IR and CR between the forward and backward electromagnetic responses. The maximum simulated IR and CR are upgraded to 12.73 dB and 0.899 at 2.64 GHz, respectively. The measured IR and CR show certain differences and peak at 2.67 GHz with

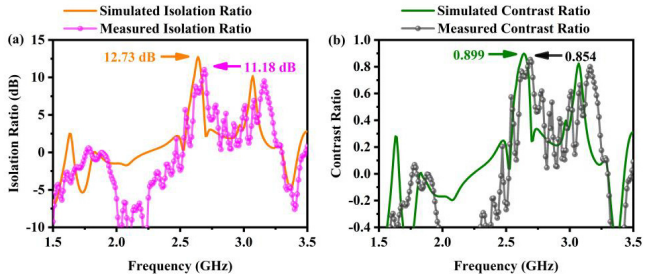

Fig. 15. Simulated and measured (a) IR and (b) CR.

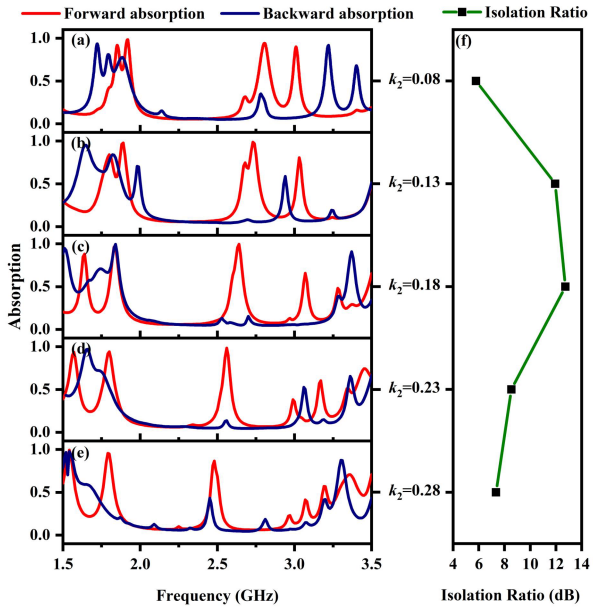

Fig. 16. Forward and backward absorptions varied with different k_2's of (a) 0.08, (b) 0.13, (c) 0.18, (d) 0.23, and (e) 0.28, and (f) their corresponding IR.

values of 11.18 dB and 0.854, whose reasons are consistent with the differences in S-parameters. This high IR has significant potential in the fields of electromagnetic compatibility, electromagnetic shielding, and improving the channel capacity of wireless communication systems.

The influences brought by the linear growth coefficient k_2 on the forward and backward absorptions are discussed in Fig. 16. With the increase of k_2 from 0.08 to 0.28, the total length of the array is gradually extended, and the forward absorption peak is shifted toward the low-frequency region. The peak values are identified as 93.58%, 98.75%, 99.53%,

Authorized licensed use limited to: Nanjing Univ of Post & Telecommunications. Downloaded on February 08,2023 at 07:48:04 UTC from IEEE Xplore. Restrictions apply.

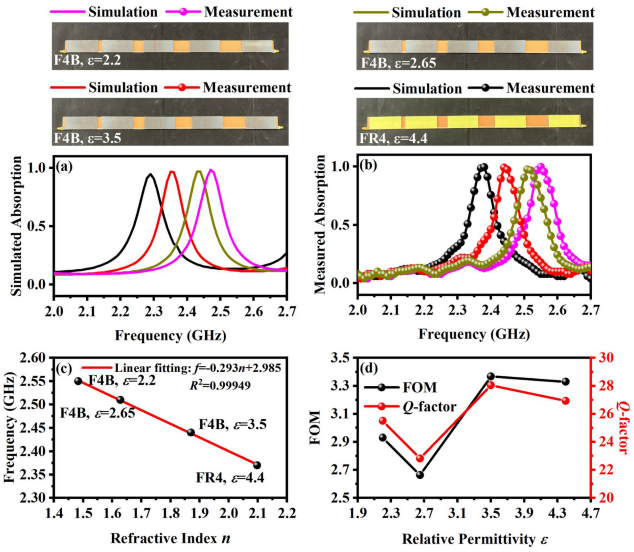

Fig. 17. (a) Simulated and (b) measured FAs with different ε's of 2.2, 2.65, 3.5, and 4.4. (c) Linear fitting curve of the measured FA peak frequencies shifted with the relative permittivity ε and refractive index n. (d) Measured Q-factor and FOM for $\varepsilon = 2.2$, $\varepsilon = 2.65$, $\varepsilon = 3.5$, and $\varepsilon = 4.4$.

98.39%, and 86.67% for $k_2 = 0.08$, $k_2 = 0.13$, $k_2 = 0.18$, $k_2 = 0.23$, and $k_2 = 0.28$, respectively. If the transmission path is overly stretched with a large k_2, it is hard for the energy radiated from the units near the starting port to completely reach and interact with the units near the ending port, where part of the energy will leak outward from both sides of the asymmetric waveguide [45]. On the other hand, if the array is overly compressed with a small k_2, the limited interference path could not provide a matching phase condition required for the coupled oscillator model to induce effective interference and sufficient absorption. These factors contribute to a first enhancing then weakening behavior of the forward absorption and a contrary behavior of the backward absorption. Furthermore, referring to transmission line theory [53], [54] and simulation results, the transmission path determined by $k_2 = 0.18$ could fulfill the condition of the impedance matching between the transmission line and loaded resonator, avoiding the occurrence of reflections and leading to a maximal forward absorption and isolation of 99.53% and 12.73 dB. Therefore, for a comprehensive consideration of the forward absorption and IR, k_2 is determined as 0.18 in this article.

IV. Permittivity Sensing Performance of Improved Nonreciprocal Metastructure Array

The enhanced near-perfect absorption peak provides a promising platform for the sensing and detecting applications, and in this article, the permittivity sensing characteristics of the proposed metastructure array are investigated in Fig. 17 by measuring the absorption responses to various relative permittivity ε of the analytes placed in the specified areas as marked by the red rectangular frame in Fig. 11. In this article, common microwave plates are adopted as the analytes, including three types of F4B plates with the relative permittivity and loss tangents of 2.2 and 0.005 [55], 2.65 and 0.0015 [56], and 3.5 and 0.002 [57], respectively, and one type of FR4 plate with the relative permittivity and loss tangent of 4.4 and 0.02 [44]. The locations of the analytes are aligned with the center of each metastructure unit, whose occupation area is slightly smaller than the dimension of the unit. All the thicknesses of the analytes are standardized to 2 mm for the convenience of fabrication. From Fig. 17(a), we can visually observe an obvious frequency redshift of the absorption peak from 2.47 to 2.29 GHz with the increased relative permittivity of the analytes. The corresponding measured results have a certain frequency deviation toward to high-frequency region compared with the simulated results. Attributed to the slight bending of the metastructure array during the measurement, it is hard to attach the analytes tightly to the array surface, and precisely for this reason, some air gaps are created between the analytes and the array surface, which is the primary trigger for this deviation to higher frequency region. Nevertheless, the phenomenon of the frequency redshift can be still detected from 2.55 to 2.38 GHz when measuring different analytes with different relative permittivities.

By extracting the measured peak data from Fig. 17(b), the linear fitting function of the forward absorption peak frequencies shifted with the refractive index n is calculated as $f = -0.293\ n + 2.985$ with a high R-squared (goodness of fit) of 0.99949, as shown in Fig. 17(c), and the sensitivity S is obtained as 0.293 GHz/RIU by (11). The excellent linearity regression degree provides firm feasibility and predictability for the applications of high-precision sensing and detection. To more comprehensively estimate the sensing performance of the proposed metastructure array, the Q-factor and FOM for the measurement of different microwave plates with various relative permittivities of 2.2, 2.65, 3.5, and 4.4 are calculated by (12) and (13) and presented in Fig. 17(d), where f_T and FWHM represent the peak frequency and full-width at half-maximum. We can be informed that the Q-factor and FOM maintain a similar volatility trend with maximum values of 28.05 and 3.37, respectively. Through (14) and (15) [58], the minimum detection limit (DL) and the minimum resolution (RS) are, respectively, calculated as 0.01485 and 0.04317. Furthermore, in the process of measuring the microwave plates with different permittivity, the forward absorption consistently remains above 0.9 while maintaining superior sensitivity and linear fitting degree, which implies excellent operating performance and stabilization of the entire absorption-based measurement system

$$S = \frac{\Delta f}{\Delta n} = \frac{\Delta f}{\Delta \sqrt{\varepsilon}} \tag{11}$$

$$Q = \frac{f_T}{\text{FWHM}} \tag{12}$$

$$\text{FOM} = \frac{S}{\text{FWHM}} \tag{13}$$

$$\text{DL} = \frac{f_T}{20SQ} \tag{14}$$

$$\text{RS} = \frac{\text{FWHM}}{1.5 \times \left(\frac{\Delta f}{\text{FWHM}}\right)^{0.25}}. \tag{15}$$

Finally, for a systematical and intuitive description of the novelty impacts, some related studies focused on EIA

Authorized licensed use limited to: Nanjing Univ of Post & Telecommunications. Downloaded on February 08,2023 at 07:48:04 UTC from IEEE Xplore. Restrictions apply.

TABLE I
COMPARISON OF RELATED STUDIES FOCUSED ON EIA AND NONRECIPROCITY PLUS THEIR EXPLORATION OF SENSING APPLICATIONS

Ref.	Function	Performance	Operating mechanism	Measured object	Operating frequency
[24]	Reciprocal EIA	Absorption:78%	Typical bright-dark-bright mode	/	0.58 THz
[38]	Reciprocal EIA and refractive index sensing	Absorption:~92%W	Two-resonators coupling	Surrounding media from n=1 to n=1.6	~ 42 THz
[9]	Nonreciprocal transmission	$\|S_{21}\|$: -5.9 dB $\|S_{12}\|$: -25.9 dB	Active transistor control	/	2.7 GHz
[39]	Nonreciprocal transmission and blood glucose monitoring	$\|S_{21}\|$: -9.8 dB $\|S_{12}\|$: -1.2 dB Sensitivity: 0.07 MHz per 1 mg/dL	Ferrimagnetic materials	Glucose levels from 0 to 82 mg/dL	27.97 GHz
[11]	Nonreciprocal absorption	Forward : ~100% Absorption Backward : ~32% Absorption	Asymmetric near-field coupling	/	224.6 THz
[40]	Nonreciprocal absorption and incident angle sensing	Forward: ~97% Absorption Backward: ~100% Reflection R-squared:0.99867 Sensitivity: 1.49 THz/degree	Black phosphorus	Incident angle from 0 ° to 70 °	630-740 THz
This work	Nonreciprocal EIUA and permittivity sensing	Forward: 99.53% Absorption Backward:5.3% Absorption R-squared: 0.99949 Sensitivity: 293 MHz/RIU	Improved bright-multiple dark-bright mode, and asymmetric spatial modulation	F4B (ε=2.2, 2.65, 3.5), FR4 (ε=4.4)	2.64 GHz

and nonreciprocity plus their exploration of sensing applications are summarized in Table I for comparison. As we can inform, the currently reported studies of the EIA effect are mostly reciprocal based on the conventional implementations of bright-dark-bright mode [24] and two-resonators coupling [59]. Few in-depth studies can be found on the nonreciprocal property of EIA. In addition, the methods of active control [9] and magnetic materials [60] still remain dominant in the current implementation of nonreciprocity, which inevitably results in high loss and complex operation. The passive nonreciprocal attempts are mainly carried out on the optical band [11], [61], which left many unexplored applications in the microwave band, especially the sensing application. We can see that the sensing studies of EIA and nonreciprocity are basically separated, and there are pretty scarce reports on the comprehensive integration of nonreciprocity, EIA, and sensing properties. In this article, our design provides a good solution to this problem. Compared with the current studies, we innovatively achieve the nonreciprocal absorption phenomenon by introducing the asymmetric spatial modulation into the conventional EIA mechanism and well enhance its commonly inadequate absorption to near-perfect absorption. Furthermore, such a near-perfect absorption peak provides a platform for the sensing property, and the permittivity sensing measurement is conducted in this article, performing greatly in the linear fitting degree and sensitivity. Such an attempt not only enriches the theoretical framework of EIA but also provides new design inspiration for realizing the nonreciprocal feature. In addition, more comparisons with other microwave sensors have been provided in Table II [62], [63], [64], [65], and we can see that the proposed design has significant advantages whether in terms of the R-square or sensitivity, and most importantly, an outstanding technical advancement is the multifunctionalization compared to other conventional microwave sensors.

TABLE II
COMPARISON WITH MORE OTHER MICROWAVE SENSORS

Ref.	f_0 (GHz)	R-square	Sensitivity (MHz)	Multi-function
[60]	1.88	0.9943	210	No
[61]	5.12 and 5.65	0.997	71	No
[62]	0.39	0.99994	54	No
[63]	2.1	0.998	72	No
This work	2.64	0.99949	293	Yes

V. CONCLUSION

In summary, to obtain nonreciprocal absorption properties, a linear incremental arrangement of five NRSs is introduced into the coupling mechanism of EIA. Such an approach is

Authorized licensed use limited to: Nanjing Univ of Post & Telecommunications. Downloaded on February 08,2023 at 07:48:04 UTC from IEEE Xplore. Restrictions apply.

equivalent to constructing an asymmetric waveguide in the forward and backward interference processes. As a result, the phenomenon of EIUA is successfully realized in the forward case, and the IR and contract ratio between the forward absorption and the backward absorption reach 10.79 dB and 0.846, respectively. To achieve a higher forward absorption for more demanding application environments, an improved nonreciprocal 1-D metastructure array is proposed and experimentally demonstrated by applying a linear quasi-periodic array configuration. The forward EIUA is enhanced to 99.53% with an IR of 12.73 dB. In addition, the permittivity sensing performance of the metastructure array is investigated by measuring four common microwave plates with different permittivities of 2.2, 2.65, 3.5, and 4.4. The measurement shows an excellent linearity regression, and the measured sensitivity, maximum FOM, minimum DL, and minimum RS are 0.293 GHz/RIU, 3.37, 0.01485, and 0.04317, respectively. This implementation is a meaningful attempt that first and systematically combines three concepts of nonreciprocity, EIA, and sensing application, offering a new design guideline and long-term implication for novel multifunctional nonreciprocal and sensing devices, and possessing potential applications in the wireless communication system, ultrasensitive sensing, one-way invisibility, and absorption-based isolator, diodes, and switch.

REFERENCES

[1] X. Guo, Y. Ding, Y. Duan, and X. Ni, "Nonreciprocal metasurface with space–time phase modulation," *Light, Sci. Appl.*, vol. 8, no. 1, p. 123, Dec. 2019.

[2] B.-I. Popa and S. A. Cummer, "Non-reciprocal and highly nonlinear active acoustic metamaterials," *Nature Commun.*, vol. 5, no. 1, Feb. 2014, Art. no. 3398.

[3] C. Liang et al., "Collision-induced broadband optical nonreciprocity," *Phys. Rev. Lett.*, vol. 125, no. 12, Sep. 2020, Art. no. 123901.

[4] M. Tamagnone et al., "Near optimal graphene terahertz non-reciprocal isolator," *Nature Commun.*, vol. 7, no. 1, Apr. 2016, Art. no. 11216.

[5] B. M. Goldsberry, S. P. Wallen, and M. R. Haberman, "Nonreciprocity and mode conversion in a spatiotemporally modulated elastic wave circulator," *Phys. Rev. A, Gen. Phys.*, vol. 17, no. 3, Mar. 2022, Art. no. 034050.

[6] M. Ishibashi, Y. Shiota, T. Li, S. Funada, T. Moriyama, and T. Ono, "Switchable giant nonreciprocal frequency shift of propagating spin waves in synthetic antiferromagnets," *Sci. Adv.*, vol. 6, no. 17, Apr. 2020, Art. no. eaaz6931.

[7] T. Goto et al., "A nonreciprocal racetrack resonator based on vacuum-annealed magnetooptical cerium-substituted yttrium iron garnet," *Opt. Exp.*, vol. 22, no. 16, pp. 19047–19054, 2014.

[8] W. Brullot, T. Swusten, and T. Verbiest, "Broadband nonreciprocal quadrupolarization-induced asymmetric transmission (Q-AT) in plasmonic nanoparticle aggregates," *Adv. Mater.*, vol. 27, no. 15, pp. 2485–2488, Apr. 2015.

[9] T. Kodera, D. L. Sounas, and C. Caloz, "Magnetless nonreciprocal metamaterial (MNM) technology: Application to microwave components," *IEEE Trans. Microw. Theory Techn.*, vol. 61, no. 3, pp. 1030–1042, Mar. 2013.

[10] Y. Shen, X. H. Deng, and L. Chen, "Unidirectional invisibility in a two-layer non-PT-symmetric slab," *Opt. Exp.*, vol. 22, no. 16, pp. 19440–19447, 2014.

[11] R. Bai, C. Zhang, X. Gu, X. R. Jin, Y. Q. Zhang, and Y. Lee, "Unidirectional reflectionlessness and perfect nonreciprocal absorption in stacked asymmetric metamaterial based on near-field coupling," *Appl. Phys. Exp.*, vol. 10, no. 11, Nov. 2017, Art. no. 112001.

[12] X.-F. Li, X. Ni, L. Feng, M.-H. Lu, C. He, and Y.-F. Chen, "Tunable unidirectional sound propagation through a sonic-crystal-based acoustic diode," *Phys. Rev. Lett.*, vol. 106, no. 8, Feb. 2011, Art. no. 084301.

[13] Z. He et al., "Asymmetric acoustic gratings," *Appl. Phys. Lett.*, vol. 98, no. 8, Feb. 2011, Art. no. 083505.

[14] R. Ramzan, M. Omar, O. F. Siddiqui, M. Amin, N. Bastaki, and T. S. Ksiksi, "Electromagnetically induced absorption in the near-field of microwave radiative elements with application to foliage moisture sensing," *IEEE Access*, vol. 6, pp. 77859–77868, 2018.

[15] A. Mouadili et al., "Electromagnetically induced absorption in detuned stub waveguides: A simple analytical and experimental model," *J. Phys., Condens. Matter*, vol. 26, no. 50, Dec. 2014, Art. no. 505901.

[16] P. Tassin, L. Zhang, R. Zhao, A. Jain, T. Koschny, and C. M. Soukoulis, "Electromagnetically induced transparency and absorption in metamaterials: The radiating two-oscillator model and its experimental confirmation," *Phys. Rev. Lett.*, vol. 109, no. 18, Oct. 2012, Art. no. 187401.

[17] Z. Shen, S. Li, Y. Xu, W. Yin, L. Zhang, and X. Chen, "Three-dimensional printed ultrabroadband terahertz metamaterial absorbers," *Phys. Rev. A, Gen. Phys.*, vol. 16, no. 1, Jul. 2021, Art. no. 014066.

[18] J. Zi et al., "Dual-functional terahertz waveplate based on all-dielectric metamaterial," *Phys. Rev. A, Gen. Phys.*, vol. 13, no. 3, Mar. 2020, Art. no. 034042.

[19] U. R. Meza, B. S. Mendoza, and W. L. Mochán, "Second-harmonic generation in nanostructured metamaterials," *Phys. Rev. B, Condens. Matter*, vol. 99, no. 12, Mar. 2019, Art. no. 125408.

[20] V. V. Cheianov, V. Fal'ko, and B. L. Altshuler, "The focusing of electron flow and a veselago lens in graphene p-n junctions," *Science*, vol. 315, no. 5816, pp. 1252–1255, Mar. 2007.

[21] Y. Sun et al., "Metamaterial analog of quantum interference: From electromagnetically induced transparency to absorption," *EPL Europhys. Lett.*, vol. 98, no. 6, Jun. 2012, Art. no. 64007.

[22] R. Taubert, M. Hentschel, J. Kästel, and H. Giessen, "Classical analog of electromagnetically induced absorption in plasmonics," *Nano Lett.*, vol. 12, no. 3, pp. 1367–1371, Mar. 2012.

[23] R. Taubert, M. Hentschel, and H. Giessen, "Plasmonic analog of electromagnetically induced absorption: Simulations, experiments, and coupled oscillator analysis," *J. Opt. Soc. Amer. B, Opt. Phys.*, vol. 30, no. 12, pp. 3123–3134, 2013.

[24] X. Zhang et al., "Electromagnetically induced absorption in a three-resonator metasurface system," *Sci. Rep.*, vol. 5, no. 1, May 2015, Art. no. 10737.

[25] L. Verslegers, Z. Yu, Z. Ruan, P. B. Catrysse, and S. Fan, "From electromagnetically induced transparency to superscattering with a single structure: A coupled-mode theory for doubly resonant structures," *Phys. Rev. Lett.*, vol. 108, no. 8, Feb. 2012, Art. no. 083902.

[26] J. He, P. Ding, J. Wang, C. Fan, and E. Liang, "Ultra-narrow band perfect absorbers based on plasmonic analog of electromagnetically induced absorption," *Opt. Exp.*, vol. 23, no. 5, pp. 6083–6091, 2015.

[27] D. Floess et al., "Plasmonic analog of electromagnetically induced absorption leads to giant thin film Faraday rotation of 14°," *Phys. Rev. X*, vol. 7, no. 2, Jun. 2017, Art. no. 021048.

[28] H.-J. Li, Y.-Z. Ren, M. Qin, and L.-L. Wang, "Multispectral perfect absorbers using plasmonically induced interference," *J. Appl. Phys.*, vol. 123, no. 20, May 2018, Art. no. 203102.

[29] A. Kik, "Complex permittivity measurement using a ridged waveguide cavity and the perturbation method," *IEEE Trans. Microw. Theory Techn.*, vol. 64, no. 11, pp. 3878–3886, Nov. 2016.

[30] H. Lobato-Morales, A. Corona-Chávez, D. V. B. Murthy, and J. L. Olvera-Cervantes, "Complex permittivity measurements using cavity perturbation technique with substrate integrated waveguide cavities," *Rev. Sci. Instrum.*, vol. 81, no. 6, Jun. 2010, Art. no. 064704.

[31] D. M. Hagl, D. Popovic, S. C. Hagness, J. H. Booske, and M. Okoniewski, "Sensing volume of open-ended coaxial probes for dielectric characterization of breast tissue at microwave frequencies," *IEEE Trans. Microw. Theory Techn.*, vol. 51, no. 4, pp. 1194–1206, Apr. 2003.

[32] A. Šarolić and A. Matković, "Dielectric permittivity measurement using open-ended coaxial probe—Modeling and simulation based on the simple capacitive-load model," *Sensors*, vol. 22, no. 16, p. 6024, Aug. 2022.

[33] H. Y. Gan, W. S. Zhao, Q. Liu, D. W. Wang, L. X. Dong, and G. F. Wang, "Differential microwave microfluidic sensor based on microstrip complementary split-ring resonator (MCSRR) structure," *IEEE Sensors J.*, vol. 20, no. 11, pp. 5876–5884, Jun. 2020.

[34] A. Kapoor, P. K. Varshney, and M. J. Akhtar, "Interdigital capacitor loaded electric-LC resonator for dielectric characterization," *Microw. Opt. Technol. Lett.*, vol. 62, no. 9, pp. 2835–2840, Sep. 2020.

Authorized licensed use limited to: Nanjing Univ of Post & Telecommunications. Downloaded on February 08,2023 at 07:48:04 UTC from IEEE Xplore. Restrictions apply.

[35] Y. Liang et al., "An LC wireless microfluidic sensor based on low temperature co-fired ceramic (LTCC) technology," *Sensors*, vol. 19, no. 5, p. 1189, Mar. 2019.

[36] E. Ekmekci and G. Turhan-Sayan, "Multi-functional metamaterial sensor based on a broad-side coupled SRR topology with a multi-layer substrate," *Appl. Phys. A, Solids Surf.*, vol. 110, no. 1, pp. 189–197, Jan. 2013.

[37] L. Zeng and H.-F. Zhang, "Absorption improvement of the anapole metastructure for sensing applications," *IEEE Sensors J.*, vol. 22, no. 12, pp. 11644–11652, Jun. 2022.

[38] K. De Vos, I. Bartolozzi, E. Schacht, P. Bienstman, and R. Baets, "Silicon-on-insulator microring resonator for sensitive and label-free biosensing," *Opt. Exp.*, vol. 15, no. 12, pp. 7610–7615, Jun. 2007.

[39] G. Govind and M. J. Akhtar, "Metamaterial-inspired microwave microfluidic sensor for glucose monitoring in aqueous solutions," *IEEE Sensors J.*, vol. 19, no. 24, pp. 11900–11907, Dec. 2019.

[40] C. Aydinalp, S. Joof, and T. Yilmaz, "Towards non-invasive diagnosis of skin cancer: Sensing depth investigation of open-ended coaxial probes," *Sensors*, vol. 21, no. 4, p. 1319, Feb. 2021.

[41] S. Taravati and G. V. Eleftheriades, "Full-duplex nonreciprocal beam steering by time-modulated phase-gradient metasurfaces," *Phys. Rev. A, Gen. Phys.*, vol. 14, no. 1, Jul. 2020, Art. no. 014027.

[42] Q. Ma et al., "Controllable and programmable nonreciprocity based on detachable digital coding metasurface," *Adv. Opt. Mater.*, vol. 7, no. 24, 2019, Art. no. 1901285.

[43] Z. Guo, Y. Sun, L. Zeng, and H. Zhang, "Temperature-controlled and photoexcited multitasking Janus metasurface in the terahertz region," *Annalen der Physik*, vol. 534, no. 5, May 2022, Art. no. 2100499.

[44] M. B. Hossain, M. R. I. Faruque, M. T. Islam, M. Singh, and M. Jusoh, "Triple band microwave metamaterial absorber based on double E-shaped symmetric split ring resonators for EMI shielding and stealth applications," *J. Mater. Res. Technol.*, vol. 18, pp. 1653–1668, May 2022.

[45] H. Kurt, D. Yilmaz, A. E. Akosman, and E. Ozbay, "Asymmetric light propagation in chirped photonic crystal waveguides," *Opt. Exp.*, vol. 20, no. 18, pp. 20635–20646, 2012.

[46] J. Zhang, K. F. MacDonald, and N. I. Zheludev, "Near-infrared trapped mode magnetic resonance in an all-dielectric metamaterial," *Opt. Exp.*, vol. 21, no. 22, pp. 26721–26728, Nov. 2013.

[47] Z. Liu et al., "Ultra-broadband tunable resonant light trapping in a two-dimensional randomly microstructured plasmonic-photonic absorber," *Sci. Rep.*, vol. 7, no. 1, Mar. 2017, Art. no. 43803.

[48] O. Siddiqui, R. Ramzan, M. Amin, and O. M. Ramahi, "A non-invasive phase sensor for permittivity and moisture estimation based on anomalous dispersion," *Sci. Rep.*, vol. 6, no. 1, Jun. 2016, Art. no. 28626.

[49] S. Hrabar, I. Krois, I. Bonic, and A. Kiricenko, "Ultra-broadband simultaneous superluminal phase and group velocities in non-foster epsilon-near-zero metamaterial," *Appl. Phys. Lett.*, vol. 102, no. 5, Feb. 2013, Art. no. 054108.

[50] A. Sellier, T. V. Teperik, and A. de Lustrac, "Resonant circuit model for efficient metamaterial absorber," *Opt. Exp.*, vol. 21, no. S6, p. A997, 2013.

[51] N. Liu et al., "Plasmonic analogue of electromagnetically induced transparency at the Drude damping limit," *Nature Mater.*, vol. 8, no. 9, pp. 758–762, Jul. 2009.

[52] C. L. G. Alzar, M. A. G. Martinez, and P. Nussenzveig, "Classical analog of electromagnetically induced transparency," *Amer. J. Phys.*, vol. 70, no. 1, pp. 37–41, Aug. 2002.

[53] Q. Liu, Z. N. Chen, Y. Liu, and C. Li, "Compact ultrawideband circularly polarized weakly coupled patch array antenna," *IEEE Trans. Antennas Propag.*, vol. 65, no. 4, pp. 2129–2134, Apr. 2017.

[54] A. Chen, Y. Zhang, Z. Chen, and S. Cao, "A Ka-band high-gain circularly polarized microstrip antenna array," *IEEE Antennas Wireless Propag. Lett.*, vol. 9, pp. 1115–1118, 2010.

[55] Z. Xu, S. Liu, S. Li, H. Zhao, L. Liu, and X. Yin, "Tunneling of spoof surface plasmon polaritons through magnetoinductive metamaterial channels," *Appl. Phys. Exp.*, vol. 11, no. 4, Apr. 2018, Art. no. 042002.

[56] B. Wang, X. Q. Lin, Y. X. Kang, and R. X. Hu, "Low-RCS broadband phased array using polarization selective metamaterial surface," *IEEE Antennas Wireless Propag. Lett.*, vol. 21, no. 1, pp. 94–98, Jan. 2022.

[57] H.-X. Xu, G.-M. Wang, Z. Tao, and T. J. Cui, "High-directivity emissions with flexible beam numbers and beam directions using gradient-refractive-index fractal metamaterial," *Sci. Rep.*, vol. 4, no. 1, p. 5744, Jul. 2014.

[58] Z. A. Zaky, B. Moustafa, and A. H. Aly, "Plasma cell sensor using photonic crystal cavity," *Opt. Quantum Electron.*, vol. 53, no. 10, p. 591, Oct. 2021.

[59] R. Ning, J. Bao, Z. Chen, and Z. Jiao, "Electromagnetically induced absorption in metamaterials and applications in the infrared range," *J. Electron. Mater.*, vol. 48, no. 7, pp. 4733–4739, Jul. 2019.

[60] A. E. Omer, A. Hojjati-Firoozabadi, S. Gigoyan, S. Safavi-Naeini, and G. Shaker, "Non-reciprocal whispering-gallery-mode resonator for sensitive blood glucose monitoring," *IEEE Trans. Instrum. Meas.*, vol. 71, pp. 1–12, 2022.

[61] Y. Ma, M. Mao, and H. Zhang, "Nonreciprocal absorption and omni-directional band gap in the biaxial hyperbolic metamaterials with black phosphorus," *J. Phys. D, Appl. Phys.*, vol. 54, no. 34, Aug. 2021, Art. no. 345103.

[62] A. M. Siddiky, M. R. I. Faruque, M. T. Islam, S. Abdullah, M. U. Khandaker, and K. S. Al-Mugren, "Dual-square-split-eing-enclosed microstrip-based sensor for noninvasive label-free detection," *Materials*, vol. 15, no. 21, p. 7688, Nov. 2022.

[63] S. Mohammadi and M. H. Zarifi, "Differential microwave resonator sensor for real-time monitoring of volatile organic compounds," *IEEE Sensors J.*, vol. 21, no. 5, pp. 6105–6114, Mar. 2021.

[64] K. Xu et al., "Novel microwave sensors based on split ring resonators for measuring permittivity," *IEEE Acesss*, vol. 6, pp. 26111–26120, 2018.

[65] A. Ebrahimi, J. Scott, and K. Ghorbani, "Differential sensors using microstrip lines loaded with two split-ring resonators," *IEEE Sensors J.*, vol. 18, no. 14, pp. 5786–5793, Jul. 2018.

Li Zeng is currently pursuing the Master degree with the College of Electronic and Optical Engineering and the College of Flexible Electronics (Future Technology), Nanjing University of Posts and Telecommunications, Nanjing, China.

His main research interests include the metastructure-based polarization converter, electromagnetically induced transparency and absorption, and multipole mode theory.

Bing-Xiang Li received the Ph.D. degree in chemical physics from the Advanced Materials and Liquid Crystal Institute, Kent State University, Kent, OH, USA, in 2019.

He is currently a Professor with the College of Electronic and Optical Engineering and the College of Flexible Electronics (Future Technology), Nanjing University of Posts and Telecommunications, Nanjing, China. His research interests include metamaterials, liquid crystals, stimuli-responsive soft materials, nonequilibrium systems, active matter, and biophysics.

Hai-Feng Zhang received the Ph.D. degree from the College of Electronic and Information Engineering, Nanjing University of Aeronautics and Astronautics, Nanjing, China, in 2014.

He is currently a Professor with the College of Electronic and Optical Engineering and the College of Flexible Electronics (Future Technology), Nanjing University of Posts and Telecommunications. His main research interests include computational electromagnetics, plasma photonic crystal, plasma stealthy, and electromagnetic properties of metamaterials.

Authorized licensed use limited to: Nanjing Univ of Post & Telecommunications. Downloaded on February 08,2023 at 07:48:04 UTC from IEEE Xplore. Restrictions apply.